



# A study of 3-D numerical simulation and comparison with experimental results on turbulent flow of venting flue gas using thermoelectric generator modules and plate fin heat sink



Jiin-Yuh Jang <sup>a,\*</sup>, Ying-Chi Tsai <sup>a</sup>, Chan-Wei Wu <sup>b</sup>

<sup>a</sup> Department of Mechanical Engineering, National Cheng-Kung University, Tainan 70101, Taiwan

<sup>b</sup> New Materials Research and Development, China Steel Corporation, Kaohsiung 81233, Taiwan

## ARTICLE INFO

### Article history:

Received 23 October 2012

Received in revised form

13 January 2013

Accepted 4 March 2013

Available online 3 April 2013

### Keywords:

Thermoelectric generator module

Plate-fin

Radiation

Waste heat recovery

## ABSTRACT

This paper investigates the three-dimensional turbulent flow in a chimney used for venting flue gas from either a boiler or stove. The thermoelectric generator (TEG) modules are embedded in the chimney walls. To understand the power output performance of the TEG module, three-dimensional numerical simulations combining convection and radiation effects, including the chimney tunnel, TEG modules, plate-fin heat sinks and cold plates, based on water cooling are developed and solved simultaneously. The effects of operational parameters such as the flue gas velocity ( $V_{in} = 3, 5$  and  $10 \text{ m/s}$ ) and flue gas temperatures ( $T_{gas} = 500, 600$  and  $700 \text{ K}$ ) on the flow and heat transfer are determined. The influences of the plate-fin height ( $H_{fin}$ ) and number of fins ( $N$ ), ranging from  $0 \text{ mm} < H_{fin} < 100 \text{ mm}$  and  $4 < N < 8$  respectively, on the power output and pressure drop are also described in detail. It is worthy of note that the net electric power ( $P_{net}$ ) of the TEG module was obtained using the ideal electric power ( $P_{TEG}$ ) minus the extra pumping power ( $P_{fan}$ ). The numerical results for the power vs. current ( $P-J$ ) curve are in good agreement with the experimental data within an error of 9%.

© 2013 Elsevier Ltd. All rights reserved.

## 1. Introduction

Thermoelectric effects include the Seebeck effect, the Peltier effect and the Thomson effect, and they are also accompanied by other effects, such as the Joule heating and Fourier heat conduction laws. Seebeck effects in semiconductor materials induce electromotive force due to temperature gradients, and Peltier effects induce temperature gradients when a DC electrical current is applied. Additionally, thermoelectric generators present potential applications in the conversion of low level thermal energy into electrical power. Especially in the case of waste heat recovery, it is unnecessary to consider the cost of thermal energy input, and there are additional advantages, such as energy savings and emission reduction, so the low efficiency problem is no longer the most important issue that needs to be taken into account [1]. In general, a thermoelectric generator (TEG) consists of a number of semiconductor pairs that are connected electrically in a series and thermally in parallel, and each pair includes a *p*-type and an *n*-type element. Although in theory, a single piece of semiconductor material could work, a series connection is used to meet the high voltage potential requirements.

*P*-type and *n*-type elements are alternated to assure that the carriers transport in the same direction.

The reported performance data is usually analyzed using conventional non-equilibrium thermodynamics [2,3]. With reference to the structure of a TEG, it has been demonstrated that a significant increase in the power output from a module can be achieved by modifying the geometry of the thermoelectric elements [4,5]. In subsequent research, Rowe [6,7] provided efficiency in a couple of solar-powered TEGs and reviewed applications of nuclear-powered TEGs in space. Chen et al. [8] used an irreversible model to study the performance of a TEG with external and internal irreversibility. The optimal range of the parameters for the device-design was determined, and the problems relative to the maximum power output and maximum efficiency were discussed. Xuan et al. [9] employed a phenomenological model to study the effects of internal and external interface layers on thermoelectric module performance. Sets of general performance formulas have also been derived. Pramanick and Das [10] performed a study on the structural design of a thermoelectric module. A model for a cascaded TEG that is based on finite time thermodynamics has also been developed. Astrain [11] used the numerical method of finite differences to evaluate the performance of the TEG system, including the heat exchangers, the heat source and the heat sink.

\* Corresponding author. Tel.: +886 6 2757575x62148; fax: +886 6 2088573.

E-mail address: [jangj@mail.ncku.edu.tw](mailto:jangj@mail.ncku.edu.tw) (J.-Y. Jang).

## Nomenclature

$A_b$	heat sink base area ( $\text{m}^2$ ) $A = L_{\text{fin}} \times L_{\text{fin}}$
$E$	electric field ( $\text{V m}^{-1}$ )
$h$	effective heat transfer coefficient ( $\text{W m}^{-2} \text{K}^{-1}$ )
$H_{\text{fin}}$	fin height (mm)
$I$	electric current (A)
$J$	electric current density ( $\text{A m}^{-2}$ )
$k$	thermal conductivity ( $\text{W m}^{-1} \text{K}^{-1}$ )
$L_{\text{fin}}$	fin length (mm)
$n$	pairs of $p$ -type and $n$ -type semiconductor
$P$	power output (W)
$P/A_b$	power density ( $\text{W m}^{-2}$ )
$\text{Pr}$	Prandtl number
$Q$	heat transfer rate (W)
$\dot{q}$	heat generation ( $\text{W m}^{-2}$ )
$R$	residual sum
$R_L$	external load resistance ( $\Omega$ )
$Re_L$	Reynolds number based on fin length
$S_{\text{fin}}$	fin spacing (mm)
$S_{\text{TEG}}$	TEG module spacing (mm)
$T$	temperature (K)
$t_b$	base thickness (mm)
$t_{\text{fin}}$	fin thickness (mm)
$V$	electric potential (V)
$V_{\text{in}}$	gas velocity ( $\text{m s}^{-1}$ )
$V_{\text{mp}}$	voltage at maximum power (V)
$V_{\text{oc}}$	open circuit voltage (V)
$x, y, z$	Cartesian coordinates

## Greek symbols

$\alpha$	Seebeck coefficient ( $\text{V K}^{-1}$ )
$\beta$	Thomson coefficient ( $\text{V K}^{-1}$ )
$\epsilon$	dissipation rate
$\epsilon_e$	extinction coefficient ( $\text{m}^{-1}$ )
$\eta$	TEG conversion efficiency (%) $\eta = P_{\text{TEG}}/Q_h$
$\kappa$	turbulent kinetic energy
$\rho$	electrical resistivity ( $\Omega \text{ m}$ )
$\sigma$	Stefan Boltzmann constant ( $\text{W m}^{-2} \text{K}^{-4}$ )
$\sigma_a$	absorption coefficient ( $\text{m}^{-1}$ )
$\sigma_s$	scattering coefficient ( $\text{m}^{-1}$ )
$\omega$	uncertainty
$\zeta$	general dependent

## Subscripts

$c$	cold side
cer	ceramic substrate
cond	conductive copper
$f$	fluid
fan	fan
gas	flue gas
$h$	hot side
net	net
$P-N$	$p$ - and $n$ -type thermoelectric semiconductor
$s$	solid
TEG	thermoelectric generator
water	cooling water

In regard to the application of thermoelectric technology in industry, there has been a growing interest in TEGs using various heat sources in power plants for combustion of waste, geothermal energy, and other industrial heat-generating processes [12,13]. Crane and Jackson [14] studied numerical heat exchanger models integrated with models for  $\text{Bi}_2\text{Te}_3$  thermoelectric modules which were validated against experimental data from previous cross-flow heat exchanger studies as well as from experiments using thermoelectric modules between counter-flow hot water and cooling air flow channels. Dai et al. [15] studied the possibility of a TEG system based on liquid metal which served to harvest and transport waste heat. The experimental results for the TEG system were discussed, and a calculated efficiency of 2% in the entire TEG system was obtained. Furthermore, in the application of the waste heat recovery power generation, there have been many conceptual designs for a power conversion system. Thacher et al. [16] investigated the feasibility of waste heat recovery from exhaust in a light truck by connecting a series of 16 TEG modules, which showed good performance at high speeds. Hsiao et al. [17] constructed a mathematical model to predict the performance of a TEG module attached to a waste heat recovery system. It was observed that the TEG module presented better performance on an exhaust pipe as opposed to a radiator. Niu et al. [18] constructed an experimental TEG unit that was used to examine the influences of the main operating conditions, hot and cold fluid inlet temperatures, flow rates and load resistance on both power output and conversion efficiency. Champier et al. [19] studied the influence of the pressure on the contact resistance between the TEG and stoves, and the experimental measurements are compared with the results of a theoretical analysis used one dimension thermoelectric model.

Because the power output of a TEG module without any heat collector is lower, to obtain high quality power output, it is feasible to insert a plate-fin heat sink into a chimney tunnel, which can

increase the convective heat transfer area and reduce thermal resistance from the flue gas to the TEG module. However, it produces a disadvantage in that the pressure drop of the system is relatively increased. Jonsson and Moshfegh [20] studied the thermal and hydraulic performance of 42 different heat sinks, including plate-fin, strip-fin, and pin-fin heat sinks, by varying the fin height, fin-to-fin distance, and the tip and lateral clearance. In addition, an empirical bypass correlation of pressure drop was proposed in their work. Lee [21] developed an analytical simulation model for predicting the thermal and pressure characteristics of fin heat sinks in a partially confined configuration. Barrett and Obinelo [22] studied straight-channel longitudinal fin heat sinks under forced air cooling. In this report, the influence of flow bypass phenomena on the thermal resistance and pressure drop across the heat sinks were also considered and discussed.

According to the literature survey on this topic [23], it is recognized that most of the previous theoretical models have been limited to one dimensional problems. However, simplified models in which the  $p-n$  element pair is simply treated as a single bulk material are not sufficient to accurately evaluate the detailed behavior of most practical fluid systems with multi-dimensional construction, irregular geometry, dynamic variations in flow field, and complicated heat transfer, nor can they precisely indicate temperature distributions and nonuniform heat flux to the TE model as the boundary condition. Only a few studies have been conducted in which a numerical analysis of a three-dimensional TEG model has been conducted. Sandoz-Rosado and Stevens [24] presented a finite element model to address three-dimensional transport in a TEG model. Simultaneously, a new method of predictive error mapping for one-dimensional analytical models was developed and demonstrated. Chen et al. [25] proposed a three-dimensional TEG model which was implemented by computational fluid dynamics commerce software (FLUENT) and its

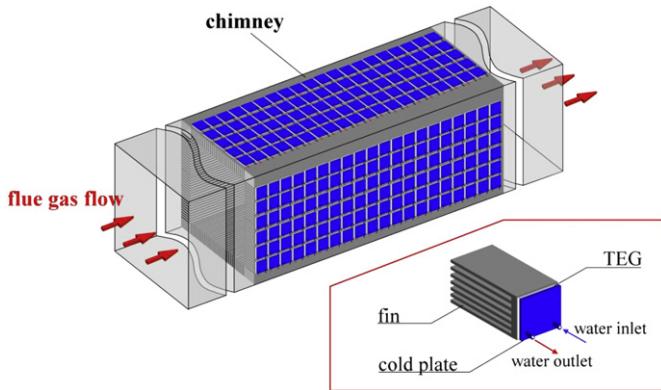


**Fig. 1.** Schematic of the thermoelectric module with a plate-fin heat sink for waste heat recovery.

user-defined functions. Cheng et al. [26] provided a three-dimensional numerical model to predict the transient thermal behavior of TECs. The results showed that both the temperatures of the hot and the cold ends increase with the cooling load and that the value of the COP (coefficient of performance) linearly increases with the cooling load. Jang et al. [27] used a numerical optimization technique in a geometrical optimization for a TEG module spreader to obtain efficient power output balancing with reasonable material costs. The results showed the optimum spreader length and thickness with the fixed module spacing for Pareto-optimal

configurations. Jang and Tsai [28] studied the optimization of TEG module spacing and its spreader thickness using a simplified conjugate-gradient method. In this report, the effects of temperature difference and waste gas heat transfer coefficients were discussed, and the numerical data were in good agreement with the experimental data.

Based on the above literature review, up to now, there have been no papers concerning the three-dimensional turbulent flow and heat transfer in a waste heat recovery system with a TEG module coupled with a plate-fin heat sink, as shown in Fig. 1. This fact has motivated the present study. The purpose of the present study is to build up a complete computational domain, including the chimney tunnel flow, the TEG module, and the plate-fin heat sink, and to directly solve the three-dimensional turbulent flow for an integral waste heat recovery system. Because of the high temperature flue gas flowing into the chimney tunnel, the radiation effect is considered. Numerical simulations focus on the effects of the geometric parameters of the plate-fin (fin height,  $H_{\text{fin}}$  and number of fins,  $N$ ) and the operational parameters (frontal velocity,  $V_{\text{in}}$  and waste gas temperatures,  $T_{\text{gas}}$ ) on the TEG module power output and on the chimney tunnel-induced pressure drop. Furthermore, an experiment is executed to verify the accuracy of the numerical results for the TEG power output.

## 2. Mathematical analysis

A schematic diagram of thermoelectric modules with a plate-fin heat sink is shown in Fig. 2. A thermoelectric module consists of a

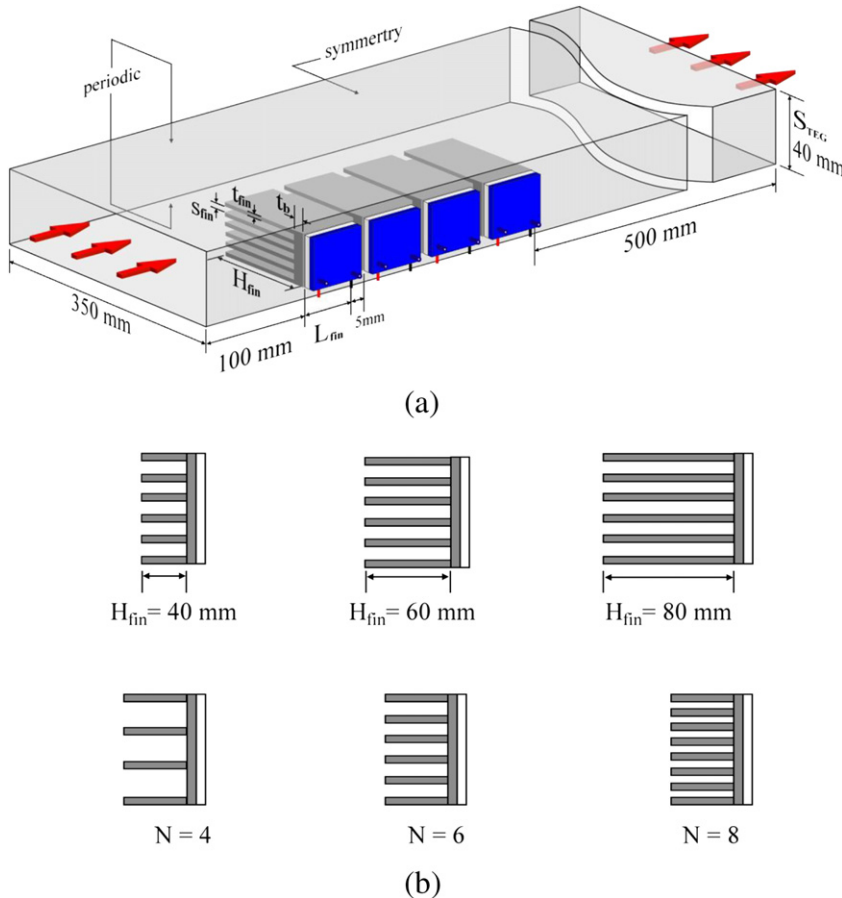


**Fig. 2.** The computational domain of the thermoelectric module (a) dimensions of the thermoelectric module (b) variables of the plate-fin heat sinks.

**Table 1**

Geometrical and thermal-electrical properties	Symbol	Value
1. Plate-fin heat sink		
Thermal conductivity (W m <sup>-1</sup> K <sup>-1</sup> )	$k_{sp}$	155 (aluminum)
Fin thickness (mm)	$t_{fin}$	1.5
Fin length (mm)	$L_{fin}$	30
Fin base thickness (mm)	$t_b$	5
2. Ceramic substrate		
Thickness (mm)	$H_{cer}$	0.75
Thermal conductance (W m <sup>-1</sup> K <sup>-1</sup> )	$k_{cer}$	49.2
3. Conductive copper		
Thickness (mm)	$H_{cond}$	0.12
Thermal conductance (W m <sup>-1</sup> K <sup>-1</sup> )	$k_{cond}$	403
Seebeck coefficient (V K <sup>-1</sup> )	$\alpha_{cond}$	$1.4 \times 10^{-5}$
Resistivity (Ω m)	$\rho_{cond}$	$1.44 \times 10^{-8}$
4. P–N thermoelectric elements (for one pair)		
Thickness (mm)	$H_{P-N}$	1.68
Thermal conductance (W m <sup>-1</sup> K <sup>-1</sup> )	$k_{P-N}$	1.6
Seebeck coefficient (V K <sup>-1</sup> )	$\alpha_{P-N}$	$\pm 2.0 \times 10^{-4}$
Electrical resistivity (Ω m)	$\rho_{P-N}$	$9.0 \times 10^{-6}$

plate-fin heat sink, a TEG and a cold plate based on water cooling. The dimensions of the assembled square TEG unit are 30 mm × 30 mm × 3.42 mm, and other detailed geometrical parameters and thermal-electrical properties of the TEG module are summarized in Table 1 [29]. The major components of flue gas from a steel plant are N<sub>2</sub> (78%), CO<sub>2</sub> (13%), H<sub>2</sub>O (6%), O<sub>2</sub> (2.6%), CO (0.2%) and SO<sub>2</sub> (0.2%). The thermophysical properties of the flue gas can be calculated as in Irvine and Liley [30], as shown in Table 2. A typical thermoelectric generator consists of many positive-type (*p*-type) and negative-type (*n*-type) semiconductor legs that are connected by copper conducting strips in serials. However, a basic thermoelectric element is composed of both a *p*-type and an *n*-type semiconductor leg. Since we use the thermoelectric models on the basis of an equivalent current method, which means there is an equal electric current and an equal cross area of thermoelectric elements, only one pair is considered here. In the present study, a TEG module with 31 pairs of *p*-type and *n*-type semiconductors is simplified to one pair. Then, the equivalent thermal-electrical properties including thermal conductivity  $k_{P-N}$ , electrical resistivity  $\rho_{P-N}$  and Seebeck coefficient  $\alpha_{P-N}$  are listed in Table 3.

**Table 2**

The thermophysical properties of the flue gas [30].

Thermophysical property	$T_{gas} = 500$ K	$T_{gas} = 700$ K
Thermal conductivity (W/m K)	$3.152 \times 10^{-5}$	$3.804 \times 10^{-5}$
Viscosity (N s/m <sup>2</sup> )	$2.171 \times 10^{-5}$	$2.553 \times 10^{-5}$
Specific heat (J/kg K)	1.0796	1.1039
Density (kg/m <sup>3</sup> )	0.9025	0.7261

**Table 3**

The equivalent thermal-electrical properties when the TEG module with *n* pairs of *p*-type and *n*-type semiconductors is simplified to one pair.

Thermo-electrical property	<i>p</i> -type and <i>n</i> -type (for one pair)	When TEG with <i>n</i> pairs is simplified to 1 pair
Thermal conductivity (W/m K)	$k_{P-N}$	$k_{P-N}$ (unchanged)
Electrical resistivity (Ω m)	$\rho_{P-N}$	$n^2 \rho_{P-N}$
Seebeck coefficient (V/K)	$\alpha_{P-N}$	$n \alpha_{P-N}$

## 2.1. Governing equations of thermoelectricity

In a thermoelectric analysis, the three-dimensional governing equations of heat and electric current in TEG at steady state can be cast into the following general form:

$$\nabla \cdot \vec{q} = \dot{q} \quad (1)$$

$$\nabla \cdot \vec{J} = 0 \quad (2)$$

In the foregoing equation, the heat flux vector  $\vec{q}$  in terms of the electric current density vector  $\vec{J}$  and Fourier's law  $k\nabla T$  are expressed as the following:

$$\vec{q} = \alpha T \vec{J} - k \nabla T \quad (3)$$

$$\vec{J} = \frac{1}{\rho} (\vec{E} - \alpha \nabla T), \quad (4)$$

where  $\vec{E} = -\nabla V$  is the electric field intensity vector, and  $V$  is the electric scalar potential. When substituting Eq. (3) into Eq. (1), the governing equation of heat flow becomes

$$\nabla \cdot (k \nabla T) - \nabla \cdot (\alpha T \vec{J}) + \dot{q} = 0. \quad (5)$$

The heat generation term  $\dot{q}$  shown in the preceding equation includes the electric power  $\vec{J} \cdot \vec{E}$  spent on Joule heating and on work against the Seebeck field  $\alpha \nabla T$ . In Eqs. (4) and (5),  $k$ ,  $\rho$  and  $\alpha$  are the thermal conductivity, electrical resistivity and Seebeck coefficient, respectively. Furthermore, with the assumptions of constant material properties  $k$  and  $\rho$ , the temperature distribution in the interior of TEG can be described by a linear second-order differential equation as

$$k \nabla^2 T - \beta \vec{J} \cdot \nabla T + \rho \vec{J}^2 = 0. \quad (6)$$

Physically, the terms appearing on the left-hand-side of the above equation represent the heat conduction, Thomson heat and Joule's heat, respectively. However, the Thomson effect is neglected because the Seebeck coefficient is independent of temperature in the present study, and thus Eq. (6) can be expressed as

$$k \nabla^2 T + \rho \vec{J}^2 = 0. \quad (7)$$

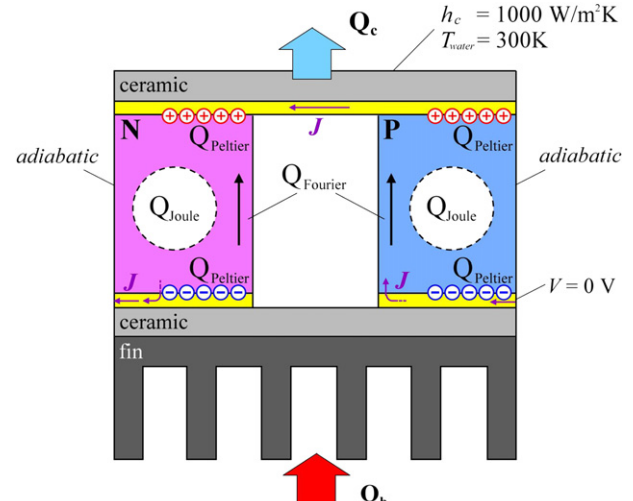


Fig. 3. Boundary condition of a thermoelectric generator module.

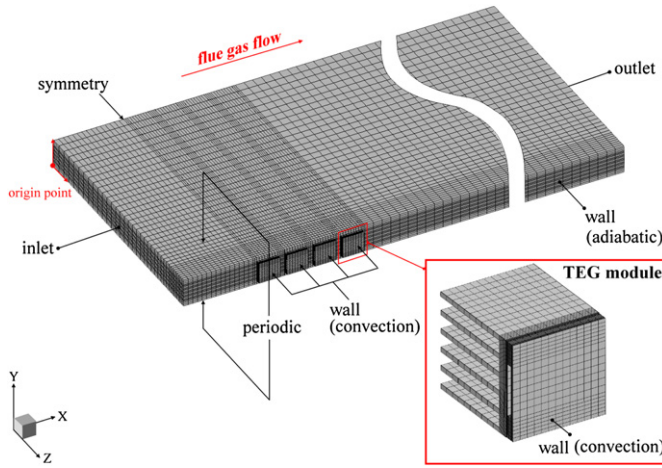


Fig. 4. Boundary condition and computational grid system of a chimney tunnel with four TEG modules.

Table 4

Comparisons between our 1-D TEG numerical solution and previous investigators [42] for  $T_h = 500$  K and  $T_c = 300$  K.

	$V_{oc}$ (volt)	$P_{max}$ (W)
Present simulation	0.023	0.03174
Fraisse et al. [42]	0.0236	0.0326
Error (%)	2.54	2.64

## 2.2. Governing equations of flow

In the present study, simulations are performed for Reynolds numbers  $Re_l$  (based on the plate-fin length ( $L_{fin}$ ) in a flow direction of 30 mm and a frontal velocity 1–10 m/s) ranging from 1000 to 10,000. Therefore, the fluid is considered incompressible with constant properties, and the flow is assumed to be a three-dimensional, steady, turbulent flow. The dimensionless equations

for mass, momentum (Reynolds-averaged Navier–Stokes equation), energy, turbulent kinetic energy,  $\kappa$ , and dissipation rate,  $\varepsilon$ , in the fluid region can be expressed in the tensor form as follows:

$$\frac{\partial \bar{u}_i}{\partial x_i} = 0 \quad (8)$$

$$\frac{\partial}{\partial x_i} \rho (\bar{u}_i \bar{u}_j) = -\frac{\partial \bar{P}}{\partial x_i} + \frac{\partial}{\partial x_j} \left[ \mu_{\text{eff}} \left( \frac{\partial \bar{u}_i}{\partial x_j} + \frac{\partial \bar{u}_j}{\partial x_i} \right) - \rho \bar{u}_i' \bar{u}_j' \right] \quad (9)$$

$$\frac{\partial}{\partial x_j} \rho C_p (\bar{u}_j \bar{T}) = \bar{u}_j \frac{\partial \bar{P}}{\partial x_j} + \bar{u}_j' \frac{\partial \bar{P}'}{\partial x_j} - \frac{\partial}{\partial x_j} \left( k \frac{\partial \bar{T}}{\partial x_j} - \rho C_p \bar{u}_j' \bar{T}' \right) - \nabla \cdot \vec{q}_r \quad (10)$$

$$\frac{\partial}{\partial x_i} (\rho \bar{u}_i \kappa) = -\frac{\partial}{\partial x_i} \left( \frac{\mu_{\text{eff}}}{\sigma_{\kappa}} \frac{\partial \kappa}{\partial x_i} \right) + \rho (\text{Pr} - \varepsilon) \quad (11)$$

$$\frac{\partial}{\partial x_i} (\rho \bar{u}_i \varepsilon) = -\frac{\partial}{\partial x_i} \left( \frac{\mu_{\text{eff}}}{\sigma_{\varepsilon}} \frac{\partial \varepsilon}{\partial x_i} \right) + \rho \frac{\varepsilon}{\kappa} \left[ \left( C_1 - C_3 \frac{\text{Pr}}{\varepsilon} \right) - C_2 \varepsilon \right], \quad (12)$$

where

$$\text{Pr} = \frac{\mu_t}{\rho} \left[ 2 \left( \frac{\partial u_i}{\partial x_i} \right)^2 - \frac{2}{3} (\nabla u_i)^2 \right], \quad \mu_{\text{eff}} = \mu + \mu_t, \quad \mu_t = \rho C_{\mu} \frac{k^2}{\varepsilon}$$

$$C_{\mu} = 0.09, \quad C_1 = 0.15, \quad C_2 = 1.90, \quad C = 0.25, \quad \sigma_{\kappa} = 0.75, \quad \text{and} \quad \sigma_{\varepsilon} = 1.15.$$

Equation (9) contains Reynolds stresses that are modeled by Chen's extended  $\kappa-\varepsilon$  turbulence model (Chen [31], Wang and Chen [32]). In Chen's model, both the production time scale and the dissipation time scale are used in closing the  $\varepsilon$  equation. This extra production time scale is claimed to allow the energy transfer mechanism of turbulence to respond to the mean strain rate more effectively. This results in an extra constant in the  $\varepsilon$  equation. As to the velocity distribution in the near-wall region ( $y^+ \leq 11.63$ ), the following law of the wall (Liakopoulos [33]) is applied:

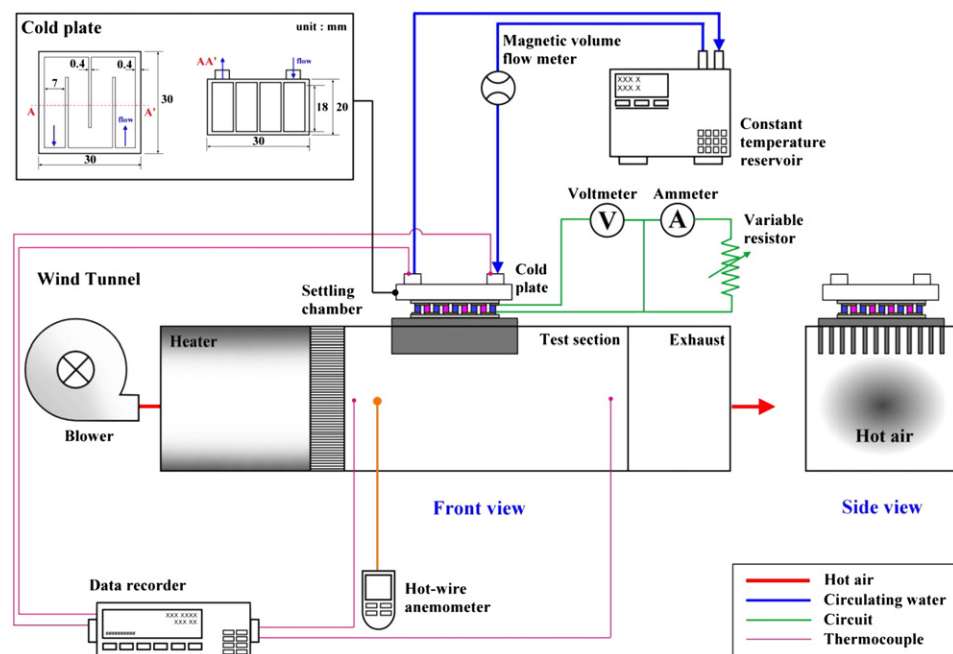


Fig. 5. Schematic diagram of the experimental setup.

$$u^+ = \ln \left[ \frac{(y^+ + 11)^{4.02}}{(y^{+2} - 7.37y^+ + 83.3)^{0.79}} \right] + 5.63 \tan^{-1} (0.12y^+ - 0.441) - 3.81, \quad (13)$$

where,

$$y^+ \equiv \frac{\rho u_\tau y}{\mu} \text{ and } u_\tau = \sqrt{\frac{\tau_w}{\rho}}. \quad (14)$$

Turbulent kinetic energy,  $\kappa$ , and dissipation rate,  $\varepsilon$ , in the near wall region can be expressed,

$$\kappa|_{y^+} = u_\tau^2 C_\mu^{-1/2} \text{ and } \varepsilon|_{y^+} = \frac{u_\tau^3 u^+}{y}. \quad (15)$$

### 2.3. Governing equations of gas radiation modeling

In the energy equation Eq. (10), in addition to the conductive and convective terms, the radiative term as the divergence of the radiative heat flux is also included. The radiative source term  $-\nabla \cdot \vec{q}_r$  is obtained by integrating the radiation intensity fields over all possible directions and wavelengths:

$$\nabla \cdot \vec{q}_r = \sigma_a \left( 4\pi I_b(\vec{r}) - \int \frac{I(\vec{r}, \vec{s})}{4\pi} d\Omega \right). \quad (16)$$

In the above equation,  $\sigma_a$  is the absorption coefficient of the flue gas. By a careful correlation of several sources of experimental data from Hottel [34], the values of the gas absorption coefficient ( $\sigma_a = 0.44$ ) are estimated.  $I(\vec{r}, \vec{s})$  is the spectral radiation intensity at the situation  $\vec{r}$  and in the direction  $\vec{s}$ . To obtain this term, it is necessary to solve the radiative transfer equation. This equation for an absorbing, emitting and scattering gray medium can be expressed as [35]:

$$(\vec{s} \cdot \nabla) I(\vec{r} \cdot \vec{s}) = -\varepsilon_e I(\vec{r} \cdot \vec{s}) + \sigma_a I_b(\vec{r}) + \frac{\sigma_s}{4\pi} \int I(\vec{r}, \vec{s}') \phi(\vec{s}, \vec{s}') d\Omega', \quad (17)$$

where  $\sigma_s$  is the scattering coefficient;  $\varepsilon_e = \sigma_a + \sigma_s$  is the extinction coefficient, and  $\phi(\vec{s}, \vec{s}')$  is the scattering phase function for the radiation from incoming direction  $\vec{s}'$  confined within the solid angle  $d\Omega'$  to scattered direction  $\vec{s}$  confined within the solid angle  $d\Omega$ . Since the scattering coefficient of gas molecules is negligible in comparison to the absorption coefficient, we neglect the effect of scattering in this calculation, that is,  $\sigma_s = 0$ . In this study, the radiative transfer equation is solved numerically by the discrete ordinates method (DOM) [36,37].

**Table 5**  
Summary of estimated uncertainties.

Primary measurements		Derived measurements		
Parameter	Uncertainties	Parameter	Uncertainties $Re_{\text{gas}} = 1000$	Uncertainties $Re_{\text{gas}} = 10,000$
$V_{\text{in}}$	0.3–1%	$Re_{\text{gas}}$	±1.2%	±0.37%
$\dot{m}_{\text{water}}$	0.5%	$Q_{\text{gas}}$	±3.5%	±1.5%
$I$	0.2%	$h_h$	±5.6%	±2.1%
$V$	0.1%	$P$	±3.2%	±3.2%
$T_{\text{gas}}$	0.1 °C			
$T_{\text{water}}$	0.05 °C			

### 2.4. Boundary conditions

Since the governing equations are elliptic in regard to spatial coordinates, it is necessary to impose boundary conditions at all of the boundaries in the computational domain. The boundary conditions and computational domains of the TEG module and the chimney tunnel are illustrated in Figs. 3 and 4, respectively. For the TEG module, the constant heat transfer coefficient  $h_c$  is specified at the cold side of the TEG, and it is estimated using the Dittus–Boelter equation [38]. In addition, the other remaining

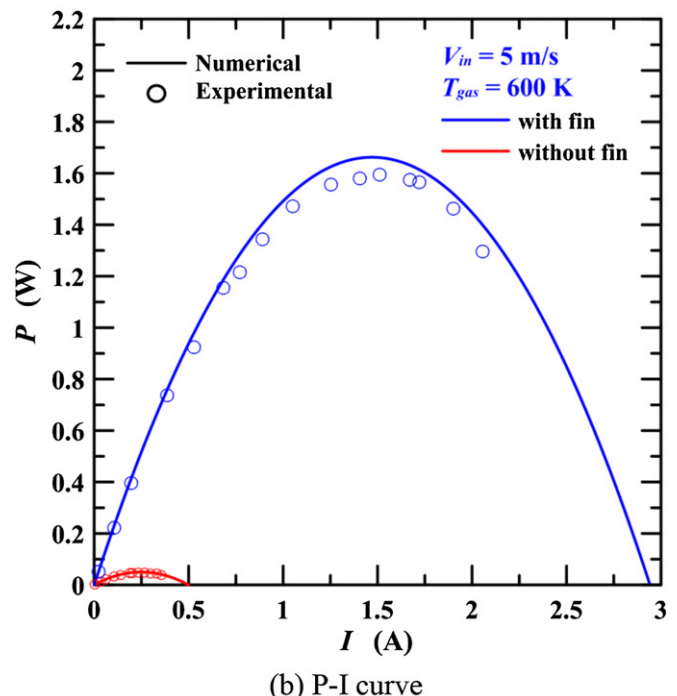
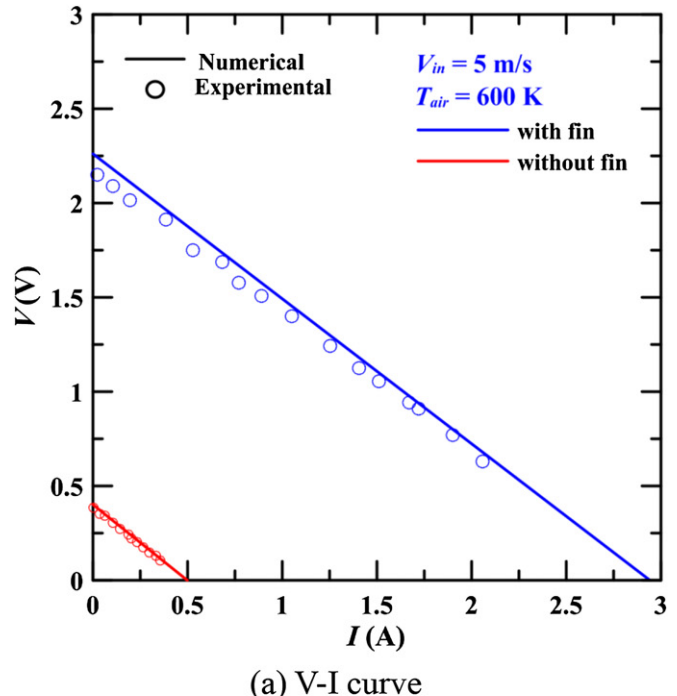


**Fig. 6.** V–I and P–I curves of experimental and numerical data with  $V_{\text{in}} = 5 \text{ m/s}$  and  $T_{\text{gas}} = 600 \text{ K}$ .

surfaces outside the chimney are set to be adiabatic. Our numerical analysis were carried for the entire range of external load resistance from  $R_L = 0$  (open circuit) to  $R_L = \infty$  (short circuit). For an open circuit situation, the voltage at the *p*-type thermoelectric element is  $V = 0$  V, and the current density at the *n*-type thermoelectric element is  $J = 0$  A/m<sup>2</sup>.

The upstream boundary of the computational domain is established at a distance of 100 mm in front of the leading edge of the first TEG module. Uniform flow with the velocity  $V_{in}$  (1–10 m/s) and temperature  $T_{in}$  (500 K, 600 K and 700 K) are assumed. For turbulent flow calculation, the inlet turbulence intensity is calculated from the following equation and is around 3%.

$$I_t \equiv \frac{u'}{u_{avg}}. \quad (18)$$

where  $u'$  is the root-mean-square of the turbulent velocity fluctuations, which is obtained from the hot-wire measurement, and  $u_{avg}$  is the mean velocity.

At the downstream end of the computational domain, located seven times the tube diameter from the last downstream row tube, the streamwise gradients (Neumann boundary conditions) for all the variables are set to zero. At the solid interface, a no-slip condition is specified. Due to the symmetry of the flow domain, calculations are performed for a half tunnel width, and a periodic match is established on both the top and bottom of the domain. Additionally, at the solid–fluid interface of heat sinks,  $T_s = T_f$ ;  $-k_s \cdot \partial T_s / \partial n = -k_f \cdot \partial T_f / \partial n$ .

For the radiative boundary conditions, the walls are assumed to emit and reflect diffusely with constant wall emissivity,  $\epsilon_w = 0.8$  [39]. In addition, the inlet and outlet sections are considered for radiative transfer to be black walls at the fluid temperatures of the inlet and outlet sections, respectively.

#### 2.4.1. Performance of a TEG

The performance of a thermoelectric generator can be characterized. The power generated from a thermoelectric generator can be calculated as follows:

$$P_{TEG} = I \cdot V. \quad (19)$$

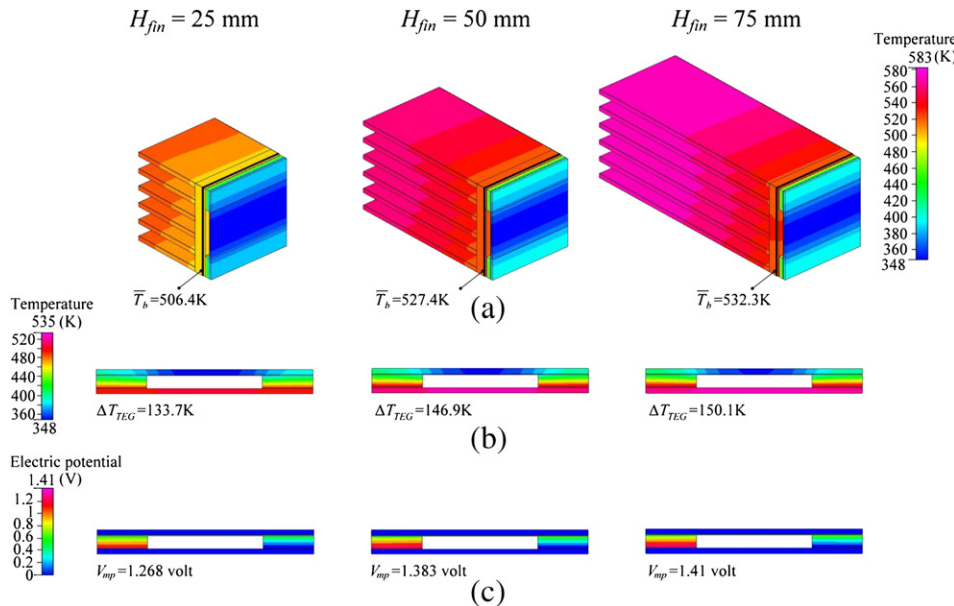


Fig. 7. The temperature and electric potential distributions of the first thermoelectric module with a plate-fin heat sink for  $N = 6$ ,  $V_{in} = 10$  m/s and  $T_{gas} = 600$  K.

The TEG conversion efficiency is given by

$$\eta = \frac{P_{TEG}}{Q_h}, \quad (20)$$

where  $Q_h$  is the heat transfer rate of the hot side.

### 3. Numerical methods

Since there is no analytical solution in this problem, the numerical simulations were carried out using a commercial CFD software package (CFD-RC) [40]. Fig. 4 illustrates the physical model and computation grid system for the TEG module with the plate-fin heat sink in Cartesian coordinates. A grid system of 83,722 grid points is typically adopted in the computational domain. Here, the grid pattern is coarsely displayed for the convenience of the reader to visualize the computational regions.

The finite-volume method was used to solve the governing equations. It involves subdividing the region in which the flow is to be solved into individual cells or control volumes so that equations can be integrated numerically on a cell-by-cell basis to produce discrete algebraic (finite-volume) equations. Several algorithms for calculating the pressure field are available in the program (SIMPLE, PISO, SIMPISO). For these steady-state computations, the SIMPLE algorithm [41] was found to give the shortest computer running times and was used in all of the calculations. Additionally, the relative error of SIMPLE algorithm compared with the other methods (PISO, SIMPISO) was within 3%.

Prior to computation, a verification of the grid-independence of the numerical solution was performed in order to ensure the accuracy and validity of the numerical results. A grid system of 83,722 grid points was typically adopted in the computational domain. In order to validate the independency of the solution on the grid, three different grid systems were investigated, which included about 61,636, 83,722 and 100,954 nodes, respectively, for a TEG module with a plate-fin heat sink in a chimney tunnel. The relative errors in the local pressure ( $P$ ), temperature ( $T$ ) and electric potential ( $V$ ) between the solutions of 83,722 and 100,954 were found to be within 3.0%. Computations were performed on an Intel Core

i7-2600 3.40G personal computer, and typical CPU times were about 6 h for each case. When the results satisfied the following conditions, the solutions were treated as converged:

$$R = \sum_{\text{domain}} |a_{nb}\zeta_{nb} + b - a_p\zeta_p| < 10^{-6} \quad (21a)$$

$$\left| \frac{\zeta_{i+1} - \zeta_i}{\zeta_i} \right| < 10^{-5}, \quad (21b)$$

where  $R$  represents the residual sum, and  $\zeta$  is a general dependent. The subscripts  $i$  and  $nb$  are the number of iterations and the neighborhood grid points, respectively.

In order to verify the accuracy of the present numerical scheme, we compared our 1-D numerical results with that by Fraisse et al. [42] for the 1-D analytical solution with  $T_h = 500$  K and  $T_c = 300$  K, as shown in Table 4. The discrepancy is less than 2.64%.

#### 4. Experimental setup and uncertainty analysis

The schematic diagram of the experimental setup is illustrated in Fig. 5. The wind tunnel system shown consists of a blower, 12 annular heaters (35 kW), a settling chamber, the TEG modules and an exhaust pipe. The air flow was driven by a 5 HP centrifugal fan with an inverter to provide various inlet velocities. During the isothermal test, it was determined that the variations in the temperature in different locations were within  $\pm 0.2$  °C and that a free stream turbulence intensity of less than 2% was achieved. The air temperatures at the inlet and the exit zones across the test section were measured using two pre-calibrated RTDs (pt-100 Ω) that had an accuracy of  $\pm 0.05$  °C. The desired air velocity through the test section was set by means of adjusting an inverter. The air velocity was measured by a hot wire with  $\pm 2.0\%$  accuracy. Furthermore, all wind tunnel systems were surrounded by insulators in order to reduce heat loss.

The TEG module was cooled with water, and its temperature was controlled at 27 °C by a thermostat reservoir. The water volumetric flow rate was measured by a magnetic volume flow meter with 0.002 L/s resolution. The heat transfer coefficients in the water channel ( $h_c$ ) could be estimated by using the Dittus–Boelter equation. A high power electrical resistor array was connected in series to the system which was used to capture the matching load for the optimized power output. The ammeter and the voltmeter were connected to measure the current in the circuit and voltage cross the external load resistor, respectively. A digital multi-meter (Fluke 170) was used to measure the voltage with an accuracy of 0.15% and the current with an accuracy of 1.0%. All the data signals were collected and converted using a data acquisition system (a hybrid recorder).

When the uncertainties in measured and calculated quantities were estimated, the bias and precision errors were both considered. These elemental errors were combined to obtain an overall uncertainty in a measured quantity using the root-sum-squares (RSS) method, which may be estimated as follows:

$$\omega_\psi = \left[ \left( \frac{\partial \psi}{\partial X_1} \right)^2 \omega_1 + \left( \frac{\partial \psi}{\partial X_2} \right)^2 \omega_2 + \dots + \left( \frac{\partial \psi}{\partial X_n} \right)^2 \omega_n \right], \quad (22)$$

where  $\omega_\psi$  is the uncertainty in the result and  $\omega_1, \omega_2, \dots, \omega_n$  are the uncertainties in the independent variables, while  $\psi$  is a given function of the independent variables,  $X_1, X_2, \dots, X_n$ . Uncertainties in the reported experimental values of the effective heat transfer coefficient ( $h$ ) and the power output ( $P$ ) were estimated using the method suggested by Moffat [43]. The uncertainties are tabulated

in Table 5. To minimize the precision uncertainty of a measurement, the experiment was measured ten times in the same way and in the same circumstances, and then the average was taken.

#### 5. Results and discussion

Fig. 6(a) and (b) show the voltage–current ( $V$ – $I$ ) and power–current ( $P$ – $I$ ) curves depicting the comparisons for the TEG module with and without a plate-fin heat sink ( $N = 6, H_{\text{fin}} = 30$  mm). The experimental results are denoted by circular symbols. For the convenience of verification of the accuracy of the numerical simulation, the work fluid is treated as hot air in the cases shown in Fig. 6. It can be seen that the predicted numerical data for the  $V$ – $I$  and  $P$ – $I$  curves are in good agreement (within 9%) with the experimental data. In addition, the results show the open circuit voltage  $V_{\text{oc}}$  to be up to 2.261 V (564% increase) for the TEG module

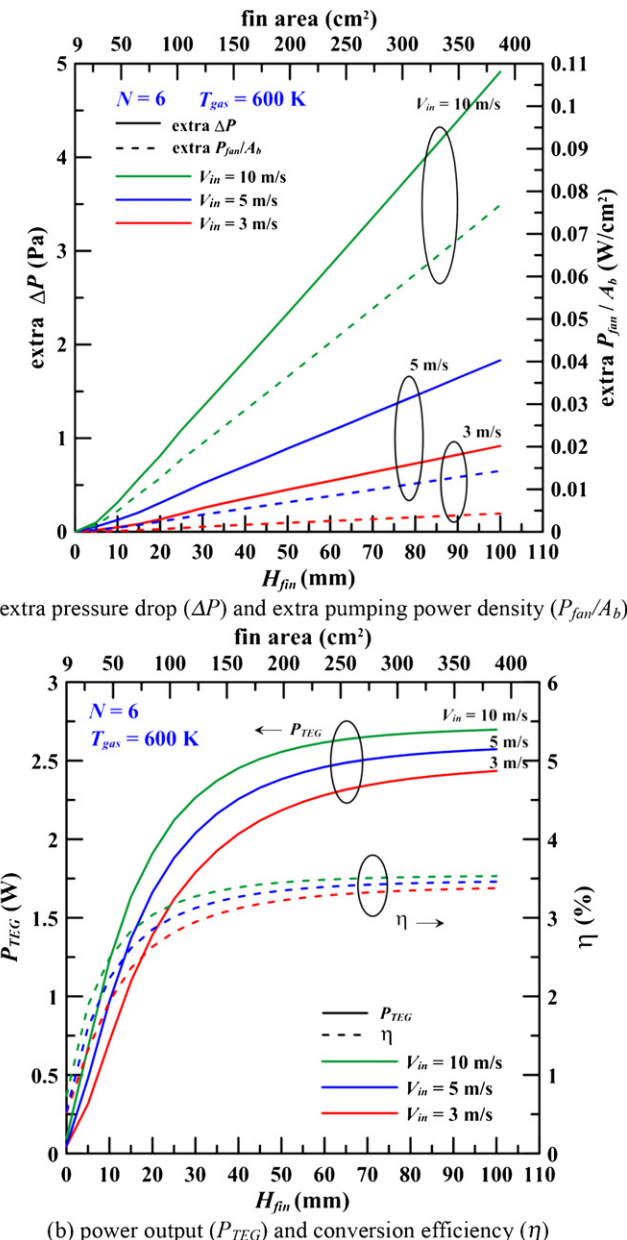


Fig. 8. The  $\Delta P$ ,  $P_{\text{fan}}/A_b$ ,  $P_{\text{TE}}$  and  $\eta$  vs. fin height ( $H_{\text{fin}}$ ) for different values of flue gas velocity with  $N = 6$  and  $T_{\text{gas}} = 600$  K.

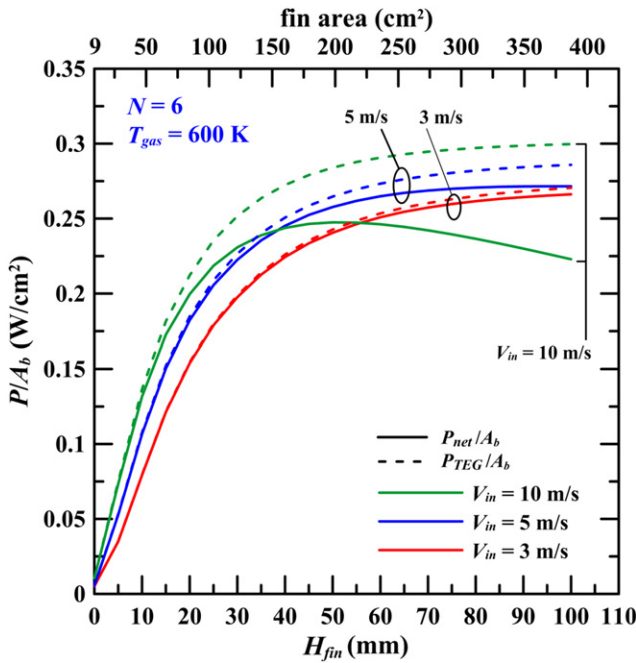


Fig. 9. The  $P_{\text{net}}/A_b$  and  $P_{\text{TEG}}/A_b$  vs. fin height ( $H_{\text{fin}}$ ) for different values of flue gas velocity with  $N = 6$  and  $T_{\text{gas}} = 600$  K.

with a plate-fin heat sink compared to that of the TEG module without a plate-fin heat sink ( $V_{\text{oc}} = 0.401$  V). It can be seen that the maximum power,  $P_{\text{TEG}}$ , occurred when the external load resistance was equal to the effective internal resistance of the TEG. A close look in Fig. 6(b) indicates that the  $P_{\text{TEG}}$  with a plate-fin heat sink can be significantly increased up to 33 times compared to that without a plate-fin heat sink.

Fig. 7(a) illustrates the temperature distribution of the first TEG module with a plate-fin heat sink for three different fin heights ( $H_{\text{fin}} = 25$  mm, 50 mm and 75 mm) at the number of fins  $N = 6$  and a flue gas velocity  $V_{\text{in}} = 10$  m/s. The cold surfaces are assumed to be

exposed to heat convection with the heat transfer coefficient  $h_c = 1000$  W/m<sup>2</sup> K, which is decided with reference to the temperature differences between an interior surface and the water temperature ( $T_{\text{water}} = 300$  K). An increase of fin height leads to intensification of the heat transfer rate. The main reasons for this are that new thermal boundary layers are developed and that the heat transfer area is increased. In this case, the predictions show that the average base temperature of the heat sink at 506.4 K, 527.4 K and 532.3 K occur at  $H_{\text{fin}} = 25$  mm, 50 mm and 75 mm, respectively. Thus, a proper heat sink size can indeed decrease the total thermal resistance due to the presence of a larger heat transfer area from the hot gas side to the cold water side. Additionally, Fig. 7(b) and (c) show the temperature and electric potential distributions of TEG for three different fin heights ( $H_{\text{fin}} = 25$  mm, 50 mm and 75 mm), respectively. It can be seen that the average temperature difference between the top and bottom surfaces of the TEG for  $H_{\text{fin}} = 75$  mm is 150.1 K, which is larger than the other two cases (133.7 K and 146.9 K). Thus, the voltage at maximum power  $V_{\text{mp}} = 1.41$  V (11% and 2.1% increase) for  $H_{\text{fin}} = 75$  mm as compared to the other two modules  $H_{\text{fin}} = 25$  mm and 50 mm, for which  $V_{\text{mp}} = 1.268$  V and 1.383 V, respectively.

Fig. 8(a) and (b) present the variations in the extra pressure drop ( $\Delta P$ ), the extra pumping power density ( $P_{\text{fan}}/A_b$ ), the ideal power output ( $P_{\text{TEG}}$ ) and the conversion efficiency ( $\eta$ ) of a TEG with the fin height of heat sink ( $H_{\text{fin}}$ ), respectively, for three different values of flue gas velocity ( $V_{\text{in}} = 3, 5$  and 10 m/s) with the number of fins  $N = 6$  and  $T_{\text{gas}} = 600$  K. As the plate-fin heat sink was inserted into the chimney tunnel, although the flue gas tended to bypass from the clearance around the fin and to redistribute itself, it undoubtedly increased the total tunnel pressure drop. As expected, the extra pressure drop and pumping power density were increased as either the fin height ( $H_{\text{fin}}$ ) or the flue gas velocity ( $V_{\text{in}}$ ) were increased. As the fin height of the heat sink went from 0 to 100 mm for  $N = 6$ , the heat transfer area increased from 9 cm<sup>2</sup> to 387 cm<sup>2</sup>. Thus, the ideal power output and conversion efficiency of the TEG was relatively increased. There is an asymptotic nature of the  $P_{\text{TEG}}$  vs.  $H_{\text{fin}}$  curves when  $H_{\text{fin}}$  is greater than 60 mm. At this time, the conversion efficiency was 3.3%, 3.4%, and 3.5% for  $V_{\text{in}} = 3, 5$  and 10 m/s, respectively.

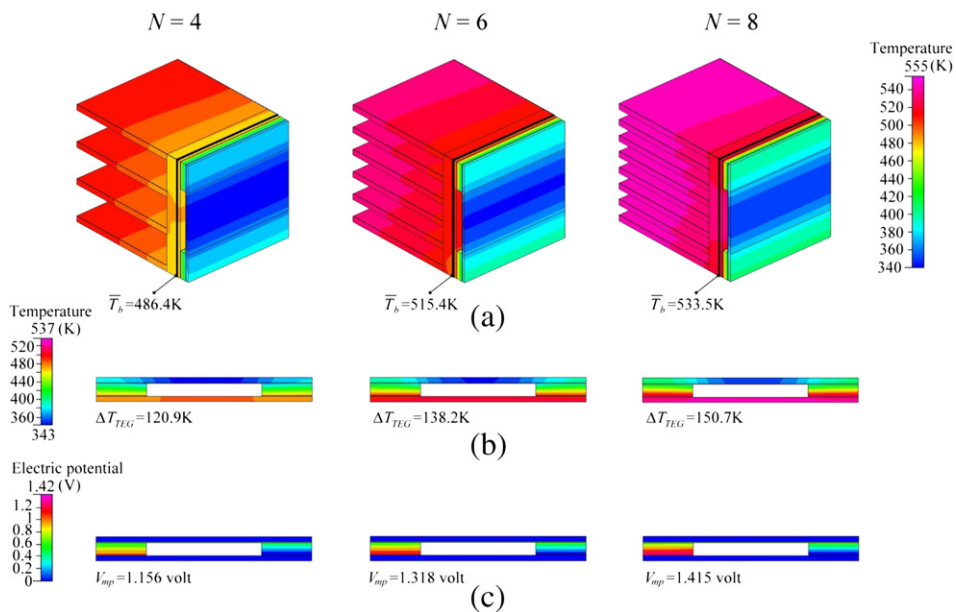


Fig. 10. The temperature and electric potential distributions of the first thermoelectric module with a plate-fin heat sink for  $H_{\text{fin}} = 30$  mm,  $V_{\text{in}} = 10$  m/s and  $T_{\text{gas}} = 600$  K.

In order to know whether or not the net electric power ( $P_{\text{net}}$ ) of the TEG module can actually generate, the extra pumping power ( $P_{\text{fan}}$ ) should be subtracted from the ideal electric power ( $P_{\text{TEG}}$ ) to obtain the actual power. As shown in Fig. 9, the effect of fin height on the net power density ( $P_{\text{net}}/A_b$ ) for three different flue gas velocities ( $V_{\text{in}} = 3, 5$  and  $10 \text{ m/s}$ ) with the same number of fins  $N = 6$  is described. The dashed lines denote the results for the ideal power density for a TEG, and the results of net power density are denoted by solid lines. When the flue gas velocity is relatively slow, the net power density doesn't exhibit notable differences with increases in the fin height of the plate-fin heat sink. However, there is a notable difference between the ideal power density and the net power density as the flue gas velocity is increased. Thus, an optimum fin height  $H_{\text{fin}}$  exists in correspondence with the maximum net power density  $P_{\text{net}}/A_b$ . As an example, the optimal fin height  $H_{\text{fin}}$  is about 50 mm for  $N = 6$ ,  $V_{\text{in}} = 10 \text{ m/s}$  and  $T_{\text{gas}} = 600 \text{ K}$ .

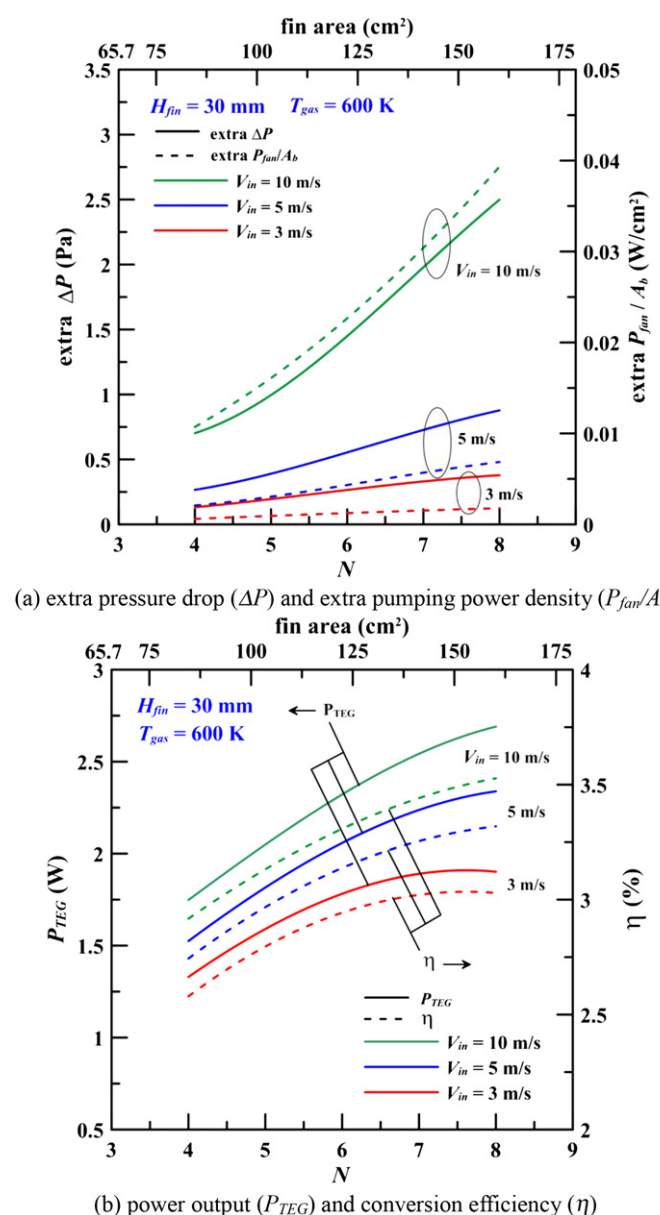


Fig. 11. The  $\Delta P$ ,  $P_{\text{fan}}/A_b$ ,  $P_{\text{TEG}}$  and  $\eta$  vs. number of fins ( $N$ ) for different values of flue gas velocity with  $H_{\text{fin}} = 30 \text{ mm}$  and  $T_{\text{gas}} = 600 \text{ K}$ .

Similarly, the performance of the TEG module with a plate-fin heat sink for different numbers of fins can be evaluated. Fig. 10(a) displays the temperature distribution of the first TEG module with a plate-fin heat sink for three different numbers of fins and a fixed fin height  $H_{\text{fin}} = 30 \text{ mm}$ . When the number of fins is increased to enlarge the heat transfer area, the heat transfer rate is relatively raised. It can be observed that the average base temperatures of the heat sinks are 486.4 K, 515.4 K and 533.5 K for  $N = 4, 6$  and 8, respectively. As can be seen in Fig. 10(b) and (c), the temperature and electric potential distributions of the TEG for three different numbers of fins ( $N = 4, 6$  and 8) are illustrated at a maximum TEG power. Respectively, the average temperature difference between the top and bottom surfaces of the TEG are 120.9 K, 138.2 K and 150.7 K for  $N = 4, 6$  and 8, respectively. The voltage values occurring at a maximum power at  $N = 8$  ( $V_{\text{mp}} = 1.415 \text{ V}$ ) increases 22% and 7.4% compared to  $N = 4$  ( $V_{\text{mp}} = 1.156 \text{ V}$ ) and  $N = 6$  ( $V_{\text{mp}} = 1.318 \text{ V}$ ).

Fig. 11(a) and (b) demonstrate the variations of the extra  $\Delta P$ ,  $P_{\text{fan}}$  and  $\eta$  with the number of the fins ( $N$ ), respectively, for three different values of flue gas velocity ( $V_{\text{in}} = 3, 5$  and  $10 \text{ m/s}$ ) with the fin height  $H_{\text{fin}} = 30 \text{ mm}$  and  $T_{\text{gas}} = 600 \text{ K}$ . As the number of fins varies from 4 to 8 in this case, the heat transfer area increases from  $84.6 \text{ cm}^2$  to  $160.2 \text{ cm}^2$ . It is evident that the extra pressure drop and the extra pumping power density are significantly increased as the number of fins ( $N$ ) is increased. Thus, it can be observed that as the number of fins is elevated from 4 to 8, the value of extra pumping power density is increased up to 3.6 times for  $V_{\text{in}} = 10 \text{ m/s}$ . Namely, the extra pumping power increases, and thus, the power generation costs are relatively raised. Additionally, the ideal power output ( $P_{\text{TEG}}$ ) and conversion efficiency ( $\eta$ ) is increased expectedly as either the number of fins ( $N$ ) or the flue gas velocity ( $V_{\text{in}}$ ) is increased.

Fig. 12 shows the effect of the number of fins ( $N$ ) on  $P_{\text{TEG}}/A_b$  and  $P_{\text{net}}/A_b$  for different values of flue gas velocity, respectively. As the number of fins increases, the net power density increases as well as the ideal power density because the increase in ideal power density is larger than the increase in extra pumping power density. It is

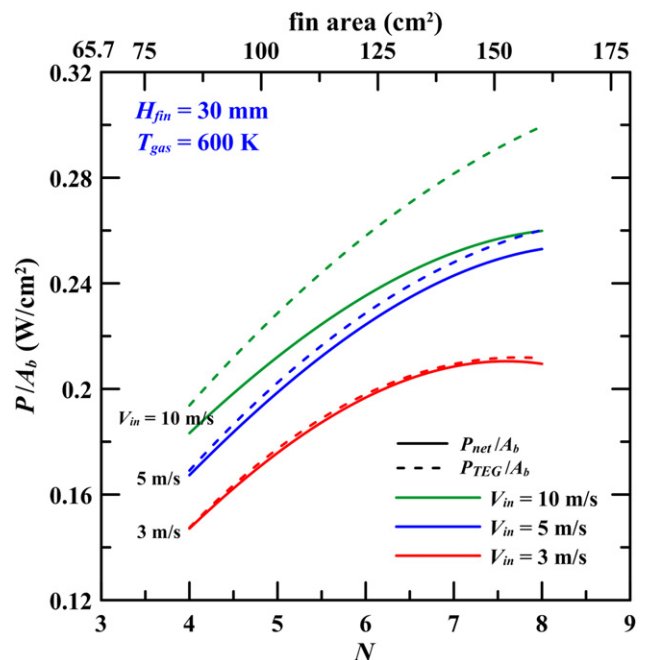


Fig. 12. The  $P_{\text{net}}/A_b$  and  $P_{\text{TEG}}/A_b$  vs. number of fins ( $N$ ) for different values of flue gas velocity with  $H_{\text{fin}} = 30 \text{ mm}$  and  $T_{\text{gas}} = 600 \text{ K}$ .

worth mentioning that the differences between the net power density and the ideal power density are enlarged with increases in the number of fins. For example, for  $H_{\text{fin}} = 30$  mm,  $T_{\text{gas}} = 600$  K and  $V_{\text{in}} = 10$  m/s, the difference between  $P_{\text{TEG}}/A_b$  and  $P_{\text{net}}/A_b$  is about  $0.011 \text{ W/cm}^2$  for  $N = 4$ , while it is enlarged to  $0.039 \text{ W/cm}^2$  for  $N = 8$ . Furthermore, as the flue gas velocity is slow ( $V_{\text{in}} = 3$  and 5 m/s), the  $P_{\text{net}}/A_b$  are very close to the  $P_{\text{TEG}}/A_b$  due to the fact that the fan pumping power density  $P_{\text{fan}}/A_b$  is relatively smaller for the lower flue gas velocity cases.

Finally, Fig. 13(a) presents the variations in the ideal power density ( $P_{\text{TEG}}/A_b$ ) of the TEG module ( $N = 6$  and  $H_{\text{fin}} = 30$  mm) vs.

the flue gas velocity ( $V_{\text{in}}$ ) for different values of flue gas temperatures ( $T_{\text{gas}} = 500, 600, 700$  K). The figure mainly shows the comparisons with radiation effect and without radiation effect. It can be seen that the values of  $P_{\text{TEG}}/A_b$  with the radiation effect are higher than those without the radiation effect. As a result, the  $P_{\text{TEG}}/A_b$  with the radiation effect is improved by an increment of 7–9% in the studied TEG module ( $N = 6$  and  $H_{\text{fin}} = 30$  mm) for slow flue gas velocity. However, the increment is lowered with increases in flue gas velocity because the forced convection effect is gradually strengthened. As seen in Fig. 13(b), the comparisons of net power density ( $P_{\text{net}}/A_b$ ) and the ideal power density ( $P_{\text{TEG}}/A_b$ ) vs. the flue gas velocity ( $V_{\text{in}}$ ) for different values of flue gas temperatures are presented. It is evident that the difference between  $P_{\text{TEG}}/A_b$  and  $P_{\text{net}}/A_b$  is enlarged with increases in the flue gas velocity, and there is an appropriate velocity for correspondence of the maximum net power density. When the flue gas velocity ( $V_{\text{in}}$ ) is increased over 6 m/s at  $T_{\text{gas}} = 700$  K, there is greater pumping power penalty over the raised power density, and therefore, the net power density may be decreased.

## 6. Conclusions

The characteristics of heat transfer behavior and power generation of a TEG module with a plate-fin heat sink are investigated numerically and experimentally, and the radiation effect of flue gas is also considered in this study. The maximum power  $P_{\text{TEG}}$  of a TEG module with a heat sink can be increased up to several dozen times as compared to a TEG module without a heat sink. The numerical results for the power vs. current ( $P-I$ ) curve are in good agreement with the experimental data within an error of 9%.

The results indicate that the extra pressure drop and pumping power density are increased with increases in fin height ( $H_{\text{fin}}$ ) and the number of fins ( $N$ ). Similarly, both the ideal electric power ( $P_{\text{TEG}}$ ) and conversion efficiency ( $\eta$ ) are also relatively increased with increases in fin height ( $H_{\text{fin}}$ ) and the number of fins ( $N$ ). It is noteworthy that the optimal fin height  $H_{\text{fin}}$  is about 50 mm for the correspondence of maximum net power density ( $P_{\text{net}}/A_b$ ) at  $N = 6$ ,  $V_{\text{in}} = 10$  m/s and that  $T_{\text{gas}} = 600$  K.

Additionally, the  $P_{\text{TEG}}/A_b$  with radiation effect increases 7–9% as compared to the  $P_{\text{TEG}}/A_b$  without radiation effect in the studied TEG module ( $N = 6$  and  $H_{\text{fin}} = 30$  mm) for slow gas velocity. However, the difference between the two is smaller with increasing flue gas velocity because the forced convection effect is gradually strengthened. The proper flue gas velocity for correspondence of maximum  $P_{\text{net}}/A_b$  exists due to the greater pumping power penalty as compared to the raised power output. The results obtained in this study should provide useful information for an industrial TEG module design for waste heat recovery.

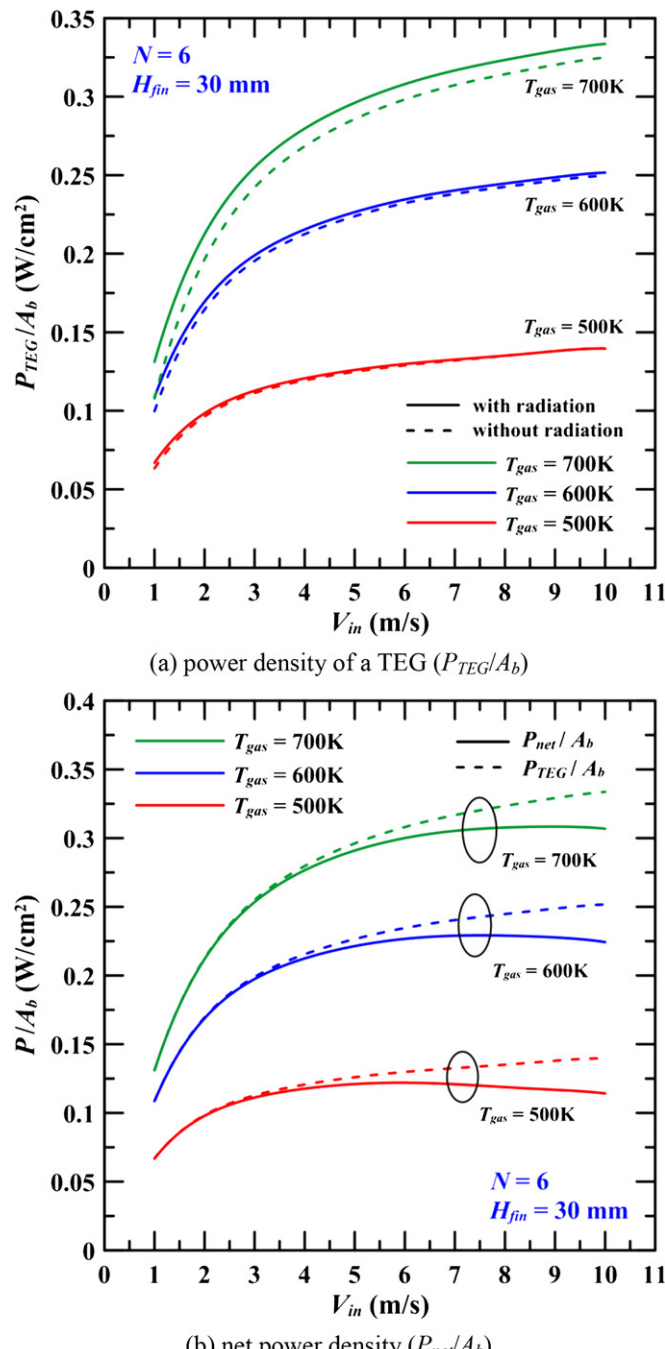
## Acknowledgments

The financial support of this work provided by the China Steel Corporation of Taiwan is appreciated.

## References

- Riffat SB, Ma XL. Thermoelectrics: a review of present and potential applications. *Appl Therm Eng* 2003;23:913–35.
- Bejan A. Advanced engineering thermodynamics. 3rd ed. Hoboken: John Wiley & Sons; 2006.
- Angrist SW. Direct energy conversion. 4th ed. Boston: Allyn and Bacon; 1992.
- Min G, Rowe DM. Optimization of thermoelectric module geometry for 'waste heat' electric power generation. *J Power Sources* 1992;38:253–9.
- Rowe DM, Min G. Evaluation of thermoelectric modules for power generation. *J Power Sources* 1998;73:193–8.
- Rowe DM. A high performance solar powered thermoelectric generator. *Appl Energy* 1981;8:269–73.

Fig. 13. The  $P_{\text{TEG}}/A_b$  and  $P_{\text{net}}/A_b$  vs. velocity ( $V_{\text{in}}$ ) for different values of flue gas temperature with  $N = 6$  and  $H_{\text{fin}} = 30$  mm.



[7] Rowe DM. Applications of nuclear-powered thermoelectric generators in space. *Appl Energy* 1991;40:241–71.

[8] Chen J, Yan Z, Wu L. The influence of Thomson effect on the maximum power output and maximum efficiency of a thermoelectric generator. *J Appl Phys* 1996;79:8823–8.

[9] Xuan XC, Ng KC, Yap C, Chua HT. A general model for studying effects of interface layers on thermoelectric devices performance. *Int J Heat Mass Transfer* 2002;45:5159–70.

[10] Pramanick AK, Das PK. Constructal design of a thermoelectric device. *Int J Heat Mass Transfer* 2006;49:1420–9.

[11] Astrain D, Vian JG, Martinez A, Rodriguez A. Study of the influence of heat exchangers thermal resistances on a thermoelectric generation system. *Energy* 2010;35:602–10.

[12] Ono K, Suzuki RO. Thermoelectric power generation: converting low-grade heat into electricity. *JOM* 1998;50:49–51.

[13] Rowe DM. Thermoelectrics, an environmentally-friendly source of electrical power. *Renew Energy* 1999;16:1251–6.

[14] Crane DT, Jackson GS. Optimization of cross flow heat exchangers for thermoelectric waste heat recovery. *Energy Conv Manag* 2004;45:1565–82.

[15] Dai D, Zhou Y, Liu J. Liquid metal based thermoelectric generation system for waste heat recovery. *Renew Energy* 2011;36:3530–6.

[16] Thacher EF, Helenbrook BT, Karri KA, Richter CJ. Testing of an automobile exhaust thermoelectric generator in a light truck. *Inst Mech Eng Part D: J Automobil Eng* 2007;221:95–107.

[17] Hsiao YY, Chang WC, Chen SL. A mathematic model of thermoelectric module with applications on waste heat recovery from automobile engine. *Energy* 2010;35:1447–54.

[18] Niu X, Yu J, Wang S. Experimental study on low-temperature waste heat thermoelectric generator. *J Power Sources* 2009;188:621–6.

[19] Champier D, Bédécarrats JP, Kousksou T, Rivaletto M, Strub F, Pignolet P. Study of a TE (thermoelectric) generator incorporated in a multifunction wood stove. *Energy* 2011;36:1518–26.

[20] Jonsson H, Moshfegh B. Modeling of the thermal and hydraulic performance of plate fin, strip fin, and pin fin heat sinks-influence of flow bypass. *IEEE Trans Compon Packag Manuf Tech* 2001;24:142–9.

[21] Lee S. Optimum design and selection of heat sinks. *IEEE Trans Compon Packag Manuf Tech A* 1995;18:812–7.

[22] Barrett AV, Obinelo IF. Characterization of longitudinal fin heat sink thermal performance and flow bypass effects through cfd methods. In: 13th IEEE SEMI-THERM Symposium 1997. p. 158–64.

[23] Minnich AJ, Dresselhaus MS, Ren ZF, Chen G. Bulk nanostructured thermoelectric materials: current research and future prospects. *Energy Environ Sci* 2009;2:466–79.

[24] Sandoz-Rosado E, Stevens RJ. Robust finite element model for the design of thermoelectric modules. *J Electron Mater* 2010;39:1848–55.

[25] Chen M, Rosendahl LA, Condra T. A three-dimensional numerical model of thermoelectric generators in fluid power systems. *Int J Heat Mass Transfer* 2011;54:345–55.

[26] Cheng CH, Huang SY, Cheng TC. A three-dimensional theoretical model for predicting transient thermal behavior of thermoelectric coolers. *Int J Heat Mass Transfer* 2010;53:2001–11.

[27] Jang JY, Tsai YC, Huang YC. Optimal design of the heat spreader applied thermoelectric module for waste heat recovery. *Adv Sci Lett* 2012;14:253–7.

[28] Jang JY, Tsai YC. Optimization of thermoelectric generator module spacing and spreader thickness used in a waste heat recovery system. *Appl Therm Eng* 2013;51:677–89.

[29] Hi-Z Technology, Inc. Available from: <http://www.hi-z.com>; 2012.

[30] Irvine TF, Liley PE. Steam and gas tables with computer equations. 1st ed. Orlando: Academic Press; 1984.

[31] Chen YS, Kim SW. Computation of turbulent flows using an extended  $k-\epsilon$  turbulence closure model 1987. NASA CR-179204.

[32] Wang TS, Chen YS. Unified Navier–Stokes flow field and performance analysis of liquid rocket engines. *AIAA J* 1993;9:678–85.

[33] Liakopoulos A. Explicit representation of the complete velocity profile in a turbulent boundary layer. *AIAA J* 1984;22:844–6.

[34] Hottel HC. Radiant heat transmission. In: McAdams WH, editor. Heat transmission. 3rd ed. New York: McGraw-Hill; 1954. Chap. 4.

[35] Modest MF. Radiative heat transfer. 2nd ed. New York: McGraw-Hill; 2003.

[36] Fiveland W. Discrete-ordinates solutions of the radiative transport equation for rectangular enclosures. *J Heat Transfer* 1984;106:699–706.

[37] Truelove J. Discrete-ordinate solutions of the radiation transport equations. *ASME J Heat Transfer* 1987;109:1048–51.

[38] Incopera FP, DeWitt DP. Fundamentals of heat and mass transfer. 5th ed. New York: John Wiley & Sons; 2002.

[39] Howell RJ, Siegel R, Menguc MP. Thermal radiation heat transfer. 5th ed. Boca Raton: CRC Press Taylor and Francis; 2010.

[40] CFD-RC. CFD Research Corporation. Alabama, USA; 2003.

[41] Van Doormal JP, Raithby GD. Enhancements of the SIMPLE method for predicting incompressible fluid flows. *Numer Heat Tran* 1984;7:147–63.

[42] Fraisse G, Ramousse J, Sgorlon D, Goupil C. Comparison of different modeling approaches for thermoelectric elements. *Energy Conv Manag* 2013;65:351–6.

[43] Moffat RJ. Describing the uncertainties in experimental results. *Exp Thermal Fluid Sci* 1988;1:3–17.